Atmos. Chem. Phys., 20, 4951–4968, 2020
https://doi.org/10.5194/acp-20-4951-2020

Atmospheric Chemistry and Physics
Open Access
EGU

Ice-nucleating ability of particulate emissions from solid-biomass-fired cookstoves: an experimental study

Kimmo Korhonen[1], Thomas Bjerring Kristensen[2], John Falk[2], Robert Lindgren[3], Christina Andersen[4], Ricardo Luis Carvalho[3,a], Vilhelm Malmborg[4], Axel Eriksson[4], Christoffer Boman[3], Joakim Pagels[4], Birgitta Svenningsson[2], Mika Komppula[5], Kari E. J. Lehtinen[1], and Annele Virtanen[1]

[1]Department of Applied Physics, University of Eastern Finland, P.O. Box 1627, 70211, Kuopio, Finland
[2]Department of Physics, Lund University, 22100, Lund, Sweden
[3]Thermochemical Energy Conversion Laboratory, Umeå University, 90187, Umeå, Sweden
[4]Ergonomics and Aerosol Technology, Lund University, P.O. Box 118, 22100, Lund, Sweden
[5]Finnish Meteorological Institute, Atmospheric Research Centre of Eastern Finland, P.O. Box 1627, 70211, Kuopio, Finland
[a]now at: Department of Environment and Planning, Centre for Environmental and Marine Studies, University of Aveiro, 3810-193, Aveiro, Portugal

Correspondence: Kimmo Korhonen (kimmo.korhonen@uef.fi)

Received: 2 October 2019 – Discussion started: 15 October 2019
Revised: 6 March 2020 – Accepted: 25 March 2020 – Published: 27 April 2020

Abstract. This research was part of the Salutary Umeå Study of Aerosols in Biomass Cookstove Emissions (SUSTAINE) laboratory experiment campaign. We studied ice-nucleating abilities of particulate emissions from solid-fuel-burning cookstoves, using a portable ice nuclei counter, Spectrometer Ice Nuclei (SPIN). These emissions were generated from two traditional cookstove types commonly used for household cooking in sub-Saharan Africa and two advanced gasifier stoves under research to promote sustainable development alternatives. The solid fuels studied included biomass from two different African tree species, Swedish softwood and agricultural residue products relevant to the region. Measurements were performed with a modified version of the standard water boiling test on polydisperse samples from flue gas during burning and size-selected accumulation mode soot particles from a 15 m^3 aerosol-storage chamber. The studied soot particle sizes in nanometers were 250, 260, 300, 350, 400, 450 and 500. From this chamber, the particles were introduced to water-supersaturated freezing conditions (−32 to −43 °C) in the SPIN.

Accumulation mode soot particles generally produced an ice-activated fraction of 10^{-3} in temperatures 1–1.5 °C higher than that required for homogeneous freezing at fixed $RH_w = 115\,\%$. In five special experiments, the combustion performance of one cookstove was intentionally modified. Two of these exhibited a significant increase in the ice-nucleating ability of the particles, resulting in a 10^{-3} ice activation at temperatures up to 5.9 °C higher than homogeneous freezing and the observed increased ice-nucleating ability. We investigated six different physico-chemical properties of the emission particles but found no clear correlation between them and increasing ice-nucleating ability. We conclude that the freshly emitted combustion aerosols form ice via immersion and condensation freezing at temperatures only moderately above homogeneous freezing conditions.

1 Introduction

Mixed-phase clouds (MPCs) play an essential role in climate and the hydrological cycle (Korolev et al., 2017; Mülmenstädt et al., 2015). Cloud droplets freeze homogeneously at temperatures near −38 °C (Pruppacher and Klett, 1997), but ice-nucleating particles (INPs) may catalyze freezing of supercooled cloud droplets at higher temperatures. A wide range of MPC properties including radiative properties and lifetime are sensitive to the formation of solid ice (Matus and L'Ecuyer, 2017), but there are significant gaps in our

knowledge regarding INP concentrations within the MPCs and these important ice formation processes.

INPs active in immersion freezing at a temperature of −30 °C are relatively rare in the lower troposphere, with concentrations on the order of 0.01 cm^{-3} in many regions (DeMott et al., 2010). Ambient INPs include dust and biological particles and potentially soot particles (Hoose and Möhler, 2012; Kanji et al., 2017). Soot particles from an acetylene burner, a kerosene burner and a soot generator have been reported to be active in immersion and condensation freezing at temperatures up to −24 (DeMott, 1990), −20 (Diehl and Mitra, 1998) and −10 °C (Gorbunov et al., 2001), respectively. However, a wide range of soot particles have been reported to be inefficient as INPs in immersion and condensation mode (e.g., Hoose and Möhler, 2012), and the available parameterizations used to estimate the soot ice-nucleating ability span several orders of magnitude (Vergara-Temprado et al., 2018). The radiative forcing associated with the impact of fossil fuel soot particles on MPCs has been reported to range from about 0.1 to about 1 Wm^{-2} depending on their ice-nucleating ability, which is uncertain (Yun et al., 2013). The Intergovernmental Panel on Climate Change (IPCC) expressed in their latest assessment report (Boucher et al., 2013) a great need for additional research with respect to the role of soot particles in heterogeneous ice nucleation (Bond et al., 2013).

Soot particles are produced from incomplete combustion (combustion with insufficient oxygen supply), and ambient soot particle properties, such as morphology and chemical composition, are highly variable and influenced by the combustion conditions and atmospheric aging (Ferry et al, 2002; Popovicheva et al., 2008; Koehler et al., 2009; Corbin et al., 2015; Mahrt et al., 2018; Bhandari et al., 2019). It is not entirely clear which soot particle properties influence the ice-nucleating ability of the particles. Chemical groups on the soot particle surface with the ability to form hydrogen bonds with water molecules are likely to be of importance (Gorbunov et al., 2001). In addition, the soot particle nanostructure may also be of importance, with highly ordered graphene structures being more efficient in supporting ice nucleation relative to lowly ordered graphene structures (Häusler et al., 2018).

Biomass combustion for cooking is an important global source of energy, being also the major environmental health risk worldwide (Lim et al., 2012). It has been estimated that approximately 2.8 billion people depend on solid-fuel combustion for daily cooking worldwide, mostly in the developing part of the world (Bonjour et al., 2013). Therefore, solid-biomass combustion is a significant source of particulate matter (PM) and soot particles on regional to global scales. However, studies of the associated ice-nucleating ability are scarce. Ambient measurements indicate that biomass combustion is a source of INPs for MPC conditions (Twohy et al., 2010; McCluskey et al., 2014), Detectable condensation and immersion freezing INP concentrations for a temperature of −30 °C have been reported for simulated wildfires in 9 of 21 and 13 of 22 experiments, respectively (Petters et al., 2009; Levin et al., 2016). Refractory black carbon has been observed to be associated with a significant fraction of the emitted INPs (Levin et al., 2016). Combustion with a modern log wood burner produced particles that acted as INPs at $T = -35$ °C but not at $T = -30$ °C for condensation and immersion freezing (Chou et al., 2013). Huang et al. (2018) modeled the indirect climate impact of solid-fueled cookstove aerosol emissions and reported a potentially significant climate impact in an increase in high clouds in their model runs where black carbon (BC) particles acted as INPs. Therefore, soot particle emissions can potentially affect MPC conditions and thus climate.

The most common way of using biomass is still in traditional cookstoves and open fires, so called three-stone fires, used in poorly ventilated spaces, resulting in severe emissions of air pollutants. However, efficient utilization of modern biomass fuels in efficient biomass cookstoves can constitute an alternative to mitigate household air pollution worldwide and the aerosol emission effect on radiative forcing (Carvalho et al., 2016). In sub-Saharan Africa, the extensive use of firewood and charcoal also leads to considerable forest and soil degradation. Thus, densification of various locally produced biomass feedstocks and residues in the form of fuel pellets can contribute to more sustainable utilization of biomass in households when comparing with the traditional harvesting and combustion of wood from natural forests (Carvalho et al., 2019). Additionally, the combustion of biomass pellets in micro-gasifier cookstoves appears to be a relatively clean solution, and their emission performance can be similar to that achieved by gas stoves (Champion and Grieshop, 2019).

In this study, we present the first measurements of the ice-nucleating ability of freshly emitted aerosol particles from biomass-fired cookstoves, and we investigated the aerosol emissions from four different cookstoves representing different advances in technology and using a wide range of biomass fuel types. The ice-nucleating ability of aerosol particles generated during standard water boiling tests under well-controlled laboratory conditions was measured online with a continuous-flow diffusion chamber (CFDC) during the Salutary Umeå Study of Aerosols in Biomass Cookstove Emissions (SUSTAINE) campaign.

2 Experiment methodology

2.1 Experiment setup

Cooking simulations were carried out at the Thermochemical Energy Conversion Laboratory (TEC-Lab) of Umeå University, and the sampling setup and relevant supporting instrumentation for the ice-nucleation (IN) experiments are presented in Fig. 1. The emissions were generated using a modified version of the standardized water boiling test (WBT,

version 4.2.4), where the cookstoves and fuels were used to heat 5 L of water from room temperature in a metal cooking pot. A typical simulation time was 60–85 min in total, including two phases of the WBT process: cold start (phase duration 15–40 min) and, after that, simmering (duration 45 min). The cooking pot was set to a designated height for each cook stove used in all but three special experiments. Solid biomass fuels were lit using 12 g of ethanol in each experiment, and water vapor from the boiling was diverted away from the sample collector dome to prevent excess humidity from entering the sampling lines. The sample aerosol was diluted by 1 : 100, cooled down to room temperature, and dried to $< 10\,\%$ RH_w using ejector dilution (marked "ED" in Fig. 1) on dry and filtered compressed air to avoid saturation of the analyzers. The supportive data were collected using multiple instruments in parallel with the CFDC instrument. Particle number size distributions were monitored during the WBT using a fast particle analyzer (FPA; Cambustion DMS500) that was connected to the transient line "A" in Fig. 1. The FPA allowed real-time monitoring of the particle size number distribution with its data output resolution of 10 Hz. Other instruments in the line A were a high-resolution time-of flight soot particle aerosol mass spectrometer (SP-AMS; Aerodyne Inc.) for measuring the physico-chemical composition of the aerosol particles and a seven-wavelength aethalometer (Magee Scientific AE33; sampling rate 1 Hz) measuring the absorption by particulate matter. The two latter instruments were connected interchangeably to the chamber sampling line "B" (Fig. 1) for chamber experiments. An SMPS system (classifier TSI 3082 equipped with aerosol neutralizer TSI 3088 and condensation particle counter – CPC, TSI 3775) measured particle number size distributions in chamber experiments at a scan range in mobility diameters from 15.7 to 615.3 nm, with continuously repeated 180 s scans during aerosol injection and sampling at an aerosol-to-sheath-flow ratio of 0.3 vs. 3 L min^{-1}, respectively. Other instruments used in chamber experiments were a cloud condensation nuclei counter (CCNC; Droplet Measurement Technologies) that sampled in parallel with an aerosol particle mass analyzer (APM, Kanomax) downstream of a differential mobility analyzer (TSI model 3071; marked DMA_{CCN} in Fig. 1) whose voltage was systematically varied for obtaining APM and CCNC scans at mobility diameters of 65, 100, 200 nm and at times also 350 nm. The time resolution of this measurement was approximately 7 min between changes in DMA_{CCN} voltage, which enabled obtainment of one APM spectrum and one to two full scan cycles on the CCNC.

The SP-AMS data were measured using dual-vaporizer measurements employing flash vaporization at 600 °C and infrared (IR) laser vaporization, followed by 70 eV electron ionization (Onasch et al., 2012). The IR laser vaporization allows detection of constituents from refractory black carbon (rBC) cores. Organic aerosol (OA) measured in this way includes non-refractory OA and refractory oxygen containing species associated with the rBC core (Corbin et al., 2015). The OA was derived from high-resolution data using the software PIKA 1.22F and included the range 13–313 amu (amu – atomic mass unit). A relative ionization efficiency of 1.4 and a collection efficiency of 1 were assumed. Information related to the soot maturity (Malmborg et al., 2019) was obtained from analysis of the refractory carbon fragments. The ratio of mid-carbon fragments (C_6^+–C_{29}^+) to the sum of all carbon fragments (C_1^+–C_{59}^+) was used as a marker of soot maturity. Information related to refractory oxygen species from the rBC cores (e.g., surface oxides) was derived from the ratio of the $C_3O_2^+$ ion to C_3^+. The $C_3O_2^+$ is exclusively detected during laser vaporization and thus not found when the laser is off. The strongest signals from surface oxides are CO^+ and CO_2^+. However, these are prone to interferences from gas phase species and non-refractory OA (Corbin et al., 2015; Nielsen et al., 2017).

The setup allowed two different types of IN experimentation: transient and chamber experiments. The transient ones were conducted during the cooking simulation where, for this purpose, sample line A of Fig. 1 was used. The purpose of transient experiments was to study the possible IN potential from fresh and polydisperse cookstove emissions during the simmering phase of the WBT. The duration of each cooking simulation was at least 30 min (simmering phase), which enabled one scan on the CFDC, over an RH range for one sampling temperature. A more detailed description of the CFDC experiments is presented in Sect. 2.4. The chamber experiments were carried out to extend sampling time up to slightly more than 2 h, and for this polydisperse aerosol was ejected into the chamber after preliminary drying and dilution so the sampling could be continued after the end of the WBTs. The chamber used in the experiments was a 15 m^3 stainless-steel aerosol-storage chamber. The chamber was purged with filtered air prior to each experiment. It was filled following the sampling setup of Fig. 1 to a mass concentration of 10–100 µg m^{-3} before the IN experiments with the CFDC were started. A typical aerosol injection time that was required to reach a sufficient mass concentration in the chamber was 10–40 min, where we aimed to have the emissions represent one full combustion cycle. After filling, the typical sampling time was approximately 2 h before the background signal of the CFDC increased too high or deposition effects, such as coagulation and wall losses, reduced the aerosol concentration too much for optimal sampling. Deposition through wall losses was strongest for ultrafine particle sizes due to diffusion, and longer sampling times were possible for accumulation mode particles only.

A CPC (Airmodus model A20) was used in parallel to the CFDC, and it recorded typical concentrations of 30–200 cm^{-3} at the 250–500 nm size range after size selection of the sample particles. The focus of the chamber experiments was to investigate the role of accumulation mode soot particles as INPs, and the samples were size-selected using a Vienna-type DMA (DMA_{IN} in Fig. 1) prior to the CFDC and the CPC, aiming for the largest particle size that was

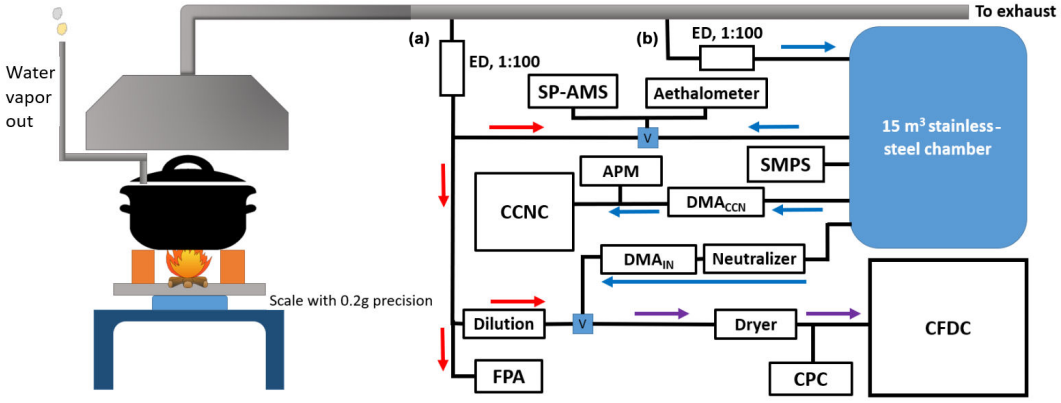

Figure 1. Schematic of the experimental setup used to conduct the WBT modified version relevant to the IN experiments. Sample lines A and B were used for transient and chamber experiments, respectively. Blue squares with letter V indicate valves which were used for switching between the sampling lines. The red and blue arrows show directions of sample flow related to transient and chamber experiments, respectively. The purple arrows show the flow direction used in both types of experiments, depending on position of the relevant switch valve. The acronyms are defined as follows: APM is aerosol particle mass analyzer, CCNC is cloud condensation nuclei counter, CFDC is continuous-flow diffusion chamber ice nucleus counter, CPC is condensation particle counter, DMA is differential mobility analyzer, ED is ejector dilution, FPA is fast particle analyzer, SMPS is scanning mobility particle sizer and SP-AMS is soot particle aerosol mass spectrometer. The dimensions and sample line lengths are not to the same scale.

present with a reasonable number concentration ($>30\,\mathrm{cm}^{-3}$). It is worth emphasizing that the chamber was used only for storing and mixing aerosol potentially representing different combustion phases, and no atmospheric aging, e.g., via oxidation or interaction with other chemicals, was applied to any emission samples that were studied using the CFDC.

2.2 Biomass feedstocks and cookstoves

The fuels used in this study consisted of firewood species available in large areas of sub-Saharan Africa and which are commonly used in residential cooking; alternatively they represent regionally relevant agricultural residues. For instance, the *Casuarina equisetifolia* (CAS), commonly known as the horsetail tree, is a species which is commonly used in agroforestry systems in the southern part of the African continent (Potgieter et al., 2014). In this work, the CAS was selected because it is a tree species that can be used in the implementation of sustainable agroforestry systems in eastern Africa. According to the Food and Agriculture Organization (FAO), agroforestry is a powerful tool in enhancing various ecosystem services, including the enhancement of food productivity, landscape regeneration and woody biomass production (Food and Agriculture Organization of the United Nations, 2017). Furthermore, the *Sesbania sesban* (SES) is also a tree applied to support the implementation of agroforestry systems, being native to most parts of sub-Saharan Africa and widespread in Kenya, where the African fuels were collected for this study.

In addition to firewood, four types of agricultural residues were studied. Africa produces annually approximately 1 million tons of coffee (International Coffee Organization, 2019), the largest coffee exporting countries being located in the sub-Saharan regions of the continent. During processing, agricultural residues such as tree branches and leaves form up to 50 % of the total weight of coffee products (Oliveira and Franca, 2015), and investigations of using these residues to support the sustainable development of sub-Saharan Africa are ongoing. The coffee husk (CH) used in this study was collected from Kenya, where *Coffea arabica* is the dominant coffee species. Moreover, bagasse (BG) is a by-product of sugar production which has also been demonstrated to be suitable for bioenergy production. This residue is usually disposed when the juice is extracted from sugarcane. In this study, we focus on the utilization of sugarcane bagasse for biomass fuel production and use, as sugarcane (*Saccharum officinarum*) is an important agricultural product in most of sub-Saharan African countries, and the biomass potential of this residue is also studied to promote sustainability. Additionally, the water hyacinth (WH), *Eichhornia crassipes*, is an indigenous species from South America, but it was introduced to Africa during the colonial period. It is a very invasive species, which requires constant population control; hence its utilization is proposed for energy purposes. Consequently, the removal of some of these plants from African lakes contributes to the sustainability of these water systems, producing significant amounts of combustible waste whose potential as a biofuel is also under research.

Furthermore, rice husk (RC) is an agricultural residue from processing African rice, *Oryza glaberrima*, when forming cereal products. Rice production has been growing

steadily in Africa for decades, and processing the plants from paddy rice to milled rice produces approximately 25 wt % of husks (Muthayya et al., 2014), whose potential as a biofuel like BG is being studied for sustainable energy use. Finally, typical Swedish softwood (SW) pellets that consist of a 50 : 50 mix between pine and spruce (*Pinus sylvestris* and *Picea abies*, respectively) were used as a reference fuel for a pelletized pure stemwood-based wooden fuel. This enabled better comparability between the emission properties. The ash-rich fuels, CH, BG, WH and RC, were mixed with SW at a 50 : 50 mass ratio to improve the suitability and combustibility of the biomass fuels for cookstove combustion applications, including better control of the ash content (i.e., certain inorganic elements). This was done to enhance the stability of the combustion process and burning time.

The simplest cookstove used was the three-stone fire (3S), which is a ring of three bricks around an open fire to hold the cooking pot above fire. The rocket stove (RS) design is an improved stove model. However, the design is also fairly simple: the fuel sticks are inserted into the fuel shelf through the horizontal metal pipe, and natural air draft causes a hot burning flame in the vertical section, just below where the cooking pot is located during operation. The more advanced concepts included two pellet gasifier stoves, where fuel pellets are loaded in a vertical pipe beneath the cooking pot and lit from above. During the operation, the pyrolysis front moves down on the fuel bed and releases volatile components. When the volatile gases reach the top of the cookstove, they are mixed with secondary air, where they create a hot burning flame beneath the cooking pot. Although the operational principle was similar in both gasifier stoves, their air supply method differs in the following way: the natural-draft gasifier stove (NDGS) uses natural air draft, while the forced-draft gasifier stove (FDGS) is equipped with an adjustable fan to force primary and secondary air flows to allow a more efficient burnout of soot and volatile organic matter.

Prior to experimentation, the fuels were pre-processed for the different types of cookstoves as follows: the fuel sticks used were chopped to pieces approximately 2 cm in diameter, 17 and 13 cm in length for the 3S and the RS, respectively, and dried at room temperature. The pellet fuels were pelletized at the TEC-Lab into dimensions of 8 mm × 15 mm (diameter × length, respectively). Fuel usage was thus standardized for the repeated WBT experiments according to cookstove type. The 3S and the RS were loaded with 100 g of stick fuel in the beginning of each WBT and refueled slowly and continuously throughout the cooking simulation to maintain the flaming combustion. A typical number of refueling events was between 5 and 10. The gasifier stoves were loaded with 1 kg of pellets before lighting the fire, since they are batch-fired appliances where fuel is not added during operation.

2.3 The CFDC instrument

Ice-nucleation experiments were conducted with the Spectrometer Ice Nuclei (SPIN; DMT Inc., Colorado, USA), described by Garimella et al. (2016). The main difference relative to the older version used by Ignatius et al. (2016) is improved temperature control via an increase in the total number of thermocouples from 8 to 32 in the main chamber (growth section).

Briefly, the SPIN is a CFDC instrument using parallel-plate geometry similar to the Portable Ice Nuclei Chamber (PINC) introduced by Chou et al. (2011) and the Zurich Ice Nuclei Chamber (ZINC) described by Stetzer et al. (2008). The sample flow at 1 standard liter per minute (SLPM) is sandwiched between two sheath flows of 4.5 SLPM each, and the residence time in the region where ice nucleation can take place is approximately 10 s. The diffusional flux of water vapor across the chamber is created via setting the ice-covered plates to different sub-zero temperatures, and the relative humidity with respect to water and ice (RH_w and RH_i, respectively) can be adjusted through the temperature difference between the plates. The aerosol is exposed to an isothermal evaporation section, upstream of the detection with an optical particle counter (OPC). The temperature of the evaporation section was set to follow the temperature of the aerosol sample in the growth section of the chamber. The temperature, relative humidities and the ideal path of the sample flow, from here on referred as lamina flow, are modeled according to a 1-D flow model by Rogers et al. (1988). The ice layer was created to the IN chamber through cooling the walls in −32 °C and filling the chamber with deionized water, which resulted in a thin layer of ice on the walls of the chamber. After filling, the IN chamber was purged of excess water and vacuumed down to 70 mbar for 3 min, which removed loose ice and reduced roughness of the ice layer and thus the background signal. Here, the background signal refers to unwanted OPC counts in the ice crystal size range, which may be due to break-up of frost on the ice-covered plates or alternatively due to tiny leaks in the instrument chamber. Typically, the background signal was below 1 particle per liter in the beginning of the experiment, and the IN chamber was re-iced when it exceeded 10–15 particles per liter. This protocol, together with averaging the instrument data over 10 s periods as was done in data analysis, allowed detection of the ice-activated fraction on the order of 10^{-6} or greater in experiments where the sample concentration exceeded 2000 cm^{-3}. Data averaging enabled investigation of large droplet and ice crystal populations against their corresponding background signals, thus decreasing the lowest detection limit.

The CPC that was operated parallel to the SPIN monitored the sample concentration and thus provided required information for calculation of the ice-activated fraction. The ice-activated fraction α is defined as

$$\alpha = \frac{N_{\mathrm{ice}}}{N_{\mathrm{CPC}}}, \tag{1}$$

where N_{ice} is the background-corrected concentration of ice crystals detected by the OPC, considering the dilution resulting from aerosol to sheath flow within SPIN, and N_{CPC} is the concentration of sample particles detected by the CPC. Background correction means that the frequency of background counts is linearly interpolated between background checks and the corresponding temporal values are subtracted from the measured signal. The uncertainty calculations in the activated fraction assume that the OPC and CPC particle counts are randomly distributed, with the standard deviation then given by the inverse of the square root of counts. The total random uncertainty of α is based on the propagation of errors of the variables involved in α calculations (Eq. 1), namely IN counts, IN background before and after each run, and the total particle count. The depicted error bars represent ± 1 standard deviation of the inferred random uncertainties.

We define the ice onset as an ice-activated fraction of 10^{-3}. Freezing conditions with $RH_w < 100\,\%$ at the lamina flow are named the deposition mode, and freezing above-water saturation is referred to as immersion freezing (Vali et al., 2015), because liquid droplet formation is expected prior to freezing. Condensation and immersion freezing modes are indistinguishable in this instrument. The experiments were carried out using automated sequences that are available in this version of the SPIN to ensure comparability between experiments on different fuels and cookstoves.

2.4 Ice-nucleation experiments

The transient experiments were performed during the modified WBT using the transient sampling line, denoted A in Fig. 1. Fresh, polydisperse emission aerosol was introduced to the SPIN after desiccation to $RH_w < 5\,\%$. The concentrations were diluted to the order of $10^3\,cm^{-3}$ to avoid vapor depletion inside the SPIN. RH scans were used for the transient experiments at constant $T = -32\,°C$, scanning the RH_i from 100 % up to 160 %, which is close to the procedure used by Petters et al. (2009) and Levin et al. (2016). This scan included studying both deposition and immersion modes because RH_w ranged from 73 % to 115 %. Two experiment scans where T was fixed at $T = -28\,°C$ had a similar RH_i range. The experimental approach for the transient experiments is a standard operation procedure often applied in previous studies (e.g., Petters et al., 2009; Welti et al., 2009).

We introduced a different experimental approach with a focus on immersion freezing for the experiments involving sampling of combustion aerosol from the chamber. This procedure is illustrated in Fig. 2, where a homogeneous freezing experiment on highly diluted ammonium sulfate (AS) droplets was performed. The dry seed particles with a mobility diameter of 350 nm were introduced to the SPIN in number concentration of approximately $150\,cm^{-3}$, and droplets formed in the growth chamber of the SPIN due to operation with supersaturated conditions on water. All experiments were carried out on similar automated T-scan ramps containing the following step. First, the internal background was checked via sampling filtered dry air for at least 5 min before the T scan began. As T descends, homogeneous freezing causes detection of ice crystals at about $-37.9\,°C$. When T reaches the lowest set point of $-43\,°C$ the background is checked again via filtering sample flow at the inlet for 3 min before opening it again and scanning the T back to $-32\,°C$ (ascending ramp). The phase change back to droplets is detected at $-38.9\,°C$, when the ice-activated fraction decreases to below 10^{-3}. The difference in ice onset and offset temperatures is most likely caused by cold pockets that may occur in the IN chamber during cooling in descending ramps. When the temperature control uncertainty is defined as 1 standard deviation from the averaged lamina temperature, it was observed that the temperatures typically deviate by 0.9–1.0 and 0.2–0.3 °C from the set value of the lamina temperature (see the shaded area around lamina temperature graph in Fig. 2) in descending and ascending ramps, respectively. Therefore, all data obtained from the descending ramps were omitted from the analysis, and only ascending ramps were studied. The total sampling time of about 2 h, which was used in chamber experiments, enabled up to three repetitions for each WBT emission sample. This sampling time allowed two to three ascending T scans for each chamber experiment, and the reproducibility of the experiments will be discussed in the Sect. 3.4.

Separation between liquid droplets and ice crystals was carried out using a basic particle-size-threshold method in the immersion mode experiments. Based on the homogeneous freezing experiments and all the other experiments we carried out with the same operation conditions, the largest droplets detected with the OPC approached a diameter of 6 µm. This can be seen in Fig. 2 between 20.38–20.49 and 20.75–20.87 h, when the inlet is open and the lamina T is above the homogeneous freezing temperature. Therefore, particles larger than 6 µm are considered ice crystals in all these experiments, and the choice of this size threshold will be discussed in Sect. 3.4.

The approach with operating the SPIN with potential coexistence of droplets and ice crystals is unusual, and it has to our knowledge previously only been applied for investigating the homogeneous freezing temperature (Ignatius et al., 2016). In this context, it should be noted that the evaporation section of the SPIN is less efficient than the ones in some other CFDCs. The SPIN OPC was designed to detect particle depolarization to be used for discrimination of droplets versus ice crystals on a particle-by-particle basis. However, we found that the depolarization data obtained with the SPIN5 OPC during this campaign were not of a quality sufficient for such an approach. We never observed any droplets with optical diameters larger than 6 µm in any experiment with the approach described above, so we found it meaningful to infer an ice-active fraction by use of that size threshold, since the ice crystal mode typically was centered around larger sizes (Fig. 2). The potential biases in the ice-active fraction as-

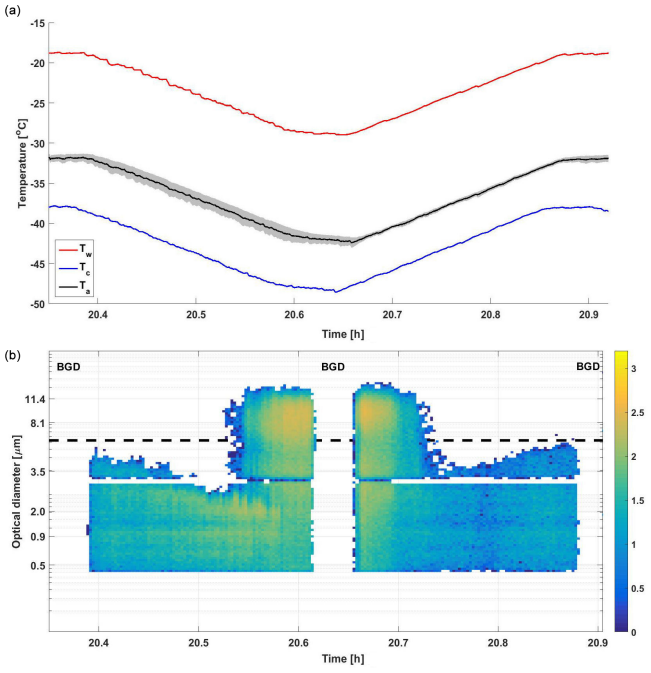

Figure 2. The immersion mode experiment procedure example from homogeneous freezing experiment with 350 nm ammonium sulfate seeds. In **(a)**, the symbols T_w, T_c and T_a represent average temperatures for warm wall, cold wall and sample aerosol (lamina), respectively. The shaded black area in the top graph represents 1 standard deviation from the averaged lamina temperature. In **(b)**, events marked "BGD" depict background signal checks. The color bar indicates the logarithmic intensity of particle counts, and the dashed black line indicates the ice threshold size of 6 µm. The gap in detection near 3 µm is a specific artifact in the OPC in this SPIN unit.

sociated with this approach are discussed in more detail in Sect. 3.4. One advantage associated with this approach was that we observed formation of a significant droplet mode for all experiments, which clearly indicated that the supersaturation sufficed to produce cloud droplets in order to investigate immersion freezing – even for particles with a low CCN activity.

The chamber experiments served two major purposes: (i) they allowed for studying aerosol emissions representing an average over several combustion phases, and (ii) they allowed for focused ice-nucleation studies of the soot particles. Considering that typical aerosol injection time was up to 40 min, the aerosol emissions from the 3S and the RS stoves are highly variable depending on the combustion phase, e.g., fuel addition, flaming and smoldering. In contrast, the aerosol emissions from the gasifier stoves were constant during most of a given transient experiment except for the ignition and the extinction phases, which allowed for SPIN scans over almost constant aerosol over time. Most aerosol injections into the aerosol-storage chamber were carried out over roughly a full combustion cycle representing the different combustion phases. Typical particle mass concentrations in the storage chamber were on the order of 10–100 µg m^{-3}, and the RH_w was typically on the order of 20 %–25 %.

The immersion mode was studied on ramps with fixed $RH_w = 115$ %, and the chamber experiments are listed in Table 2. In a few selected experiments, we investigated how modified combustion conditions possibly would influence the ice-nucleating activity of the emitted soot particles. Five different modified experiments with the FDGS and SW pellets were used to inject aerosol particles into the chamber from which SPIN sampled size-selected soot particles. Two of them were carried out with the secondary air supply being intentionally blocked, and the pot height was adjusted to increase the particle size in three experiments. In the experiments with blocked secondary air supply, the FDGS was modified to simulate usage of a poorly functioning stove, and the experiment was repeated twice on SW fuel. This simulation was done by reducing the secondary air supply, which resulted in more inefficient and incomplete combustion and increased the production of large soot particles significantly. The "pot height" experiments were done using different, less favorable heights of the cooking pot. The three such experiments were done on designated operation conditions of the FDGS and SW pellets, but the cooking pot was intentionally lifted to achieve production of larger particles: the real-time size distribution was monitored on the FPA throughout the experiment, and the pot height was adjusted in a way that an increased production of large soot particles was observed. In typical cases, an offset of 8–10 cm above the designated pot height affected production of large soot particles significantly.

It has previously been shown that the CFDC ice concentrations are often biased low by a factor of 3 and potentially up to a factor of 10, depending on the operation conditions (DeMott et al., 2015, 2017; Garimella et al., 2017). This bias is due to non-ideal behavior of instruments, when the sample and sheath flows cannot follow the theoretical streamlines ideally. Hence, we will also estimate this effect and its possible effect on the results of this study.

2.5 Emission particle characterization

It is still largely an open question which soot particle parameters influence the ice-nucleating ability. However, the extensive online characterization of the aerosol applied in this work allowed us to investigate such potential links. The CCN activity, reported as the apparent hygroscopicity parameter κ_a, was inferred as described by Petters and Kreidenweis (2007) and the effective density ρ_e in a similar fashion as done by Rissler et al. (2013). The aethalometer was used for studying optical properties of the emission particles, measuring the absorption Ångström exponent (AAE) in the wavelength interval from 370 to 950 nm. Furthermore, three physico-chemical properties were inferred from the SP-AMS

Table 1. Summary of transient experiments on polydisperse sample particles on RH_i scan 100 %–160 % and the ice crystal detection limit. The detection limit depends on sample concentration and is defined as the lowest activated fraction when detection of ice crystals is distinguishable from the background signal in data averaged over 10 s periods.

Cookstove	Fuel	Temperature	Detection limit
Three-stone fire	BIR	−32 °C	6.6×10^{-6}
Rocket stove	CAS	−32 °C	7.3×10^{-6}
Rocket stove	CAS	−32 °C	4.0×10^{-6}
ND gasifier	SW	−32 °C	5.0×10^{-6}
ND gasifier	CH + SW	−32 °C	1.3×10^{-6}
ND gasifier	BG + SW	−28 °C	5.0×10^{-6}
ND gasifier	BG + SW	−32 °C	3.4×10^{-6}
FD gasifier	SW	−32 °C	1.2×10^{-5}
FD gasifier	BG + SW	−32 °C	6.2×10^{-6}
FD gasifier	WH + SW	−32 °C	3.9×10^{-6}
FD gasifier	RC + SW	−32 °C	4.4×10^{-6}

measurements: the ratio of organic aerosol to black carbon (OA / BC), relative abundance of refractory oxygen species and indirect information about the nanostructure of soot particles (Malmborg et al., 2019). The aim of this characterization was to study if the aforementioned six physico-chemical properties can explain variability in IN abilities from repeated experiments on different cookstoves, fuels and combustion conditions.

3 Results and discussion

We present the IN results from transient and chamber experiments, compared to homogeneous freezing experiments whenever the experimentation included sample temperatures near or below homogeneous freezing temperature from the droplet freezing test. A result is considered positive if heterogeneous ice nucleation is observed under freezing conditions that are distinguishable from homogeneous freezing and negative if ice crystals have not been observed or if there is no distinguishable difference to homogeneous freezing conditions.

3.1 Transient experiments

Transient experiments are summarized in Table 1, and they all were conducted on fresh, polydisperse samples whose size distributions were measured simultaneously during the WBTs. All samples were dominated by ultrafine (< 100 nm) particles by number, and the fraction of particles larger than 250 nm was typically below 5 % of the total particle number concentration in all experiments. It can be expected that the size distributions and emission properties varied more on the 3S and the RS than on gasifier stoves due to refueling, i.e., addition of fuel sticks during the simmering phase. Considering that the particle number concentration introduced to the SPIN was typically 1000–2500 cm^{-3} in transient experiments, ice nucleation was detectable with ice-active fractions on the order of 10^{-6} or greater. Large accumulation mode particles accounted for concentrations up to about 100 cm^{-3} within the used sample concentrations. Ice crystal formation was not observed within the detection limit in any experiment at $T = -32$ °C or above. These 11 observations indicate that the fresh aerosol emissions from these four stoves are active ice nucleators in neither the deposition nor immersion and condensation mode at the given experiment temperatures. The emissions from all experiments were dominated by ultrafine particles by number, which clearly had no contribution to heterogeneous ice nucleation for the given temperatures.

Table 2. Summary of chamber experiments. The pot height experiments represent modified combustion conditions when the cooking pot was intentionally placed above the designated height of the respective cookstove. The doubly charged particle fractions and sizes are determined following Wiedensohler (1988). In cases where the measurements were not performed in the size range relevant for multiply charged particles, the estimates are obtained using lognormal fits to the detected parts of the soot modes.

Cookstove	Fuel	Sample size (nm)	Doubly charged fraction
Three-stone fire	SES	250	0.08
Three-stone fire	CAS	300	0.08
Three-stone fire	CAS	500	0.03
Rocket stove	CAS	250	0.20
Rocket stove	CAS	350	0.06
Rocket stove	CAS	450	0.04
ND gasifier	SW	400	–
FD gasifier	CH + SW	260	0.13
Modified FD gasifier	SW	450	0.08
Modified FD gasifier	SW	500	0.06
FD gasifier, pot height no. 1	SW	400	0.1
FD gasifier, pot height no. 2	SW	400	0.18
FD gasifier, pot height no. 3	SW	500	–

3.2 Chamber experiments

The particle number size distributions were measured using the SMPS from the storage chamber, and therefore the sample sizes, as Fig. 3 shows, are based on dry particle mobility. The number size distributions were typically highly dominated by ultrafine and largely inorganic hygroscopic particles, as indicated by CCN measurements (although not presented in this study). All ice-nucleation experiments involving polydisperse aerosol indicated that the ultrafine particles did not play a role as INPs for the investigated conditions. The chamber experiments focused on

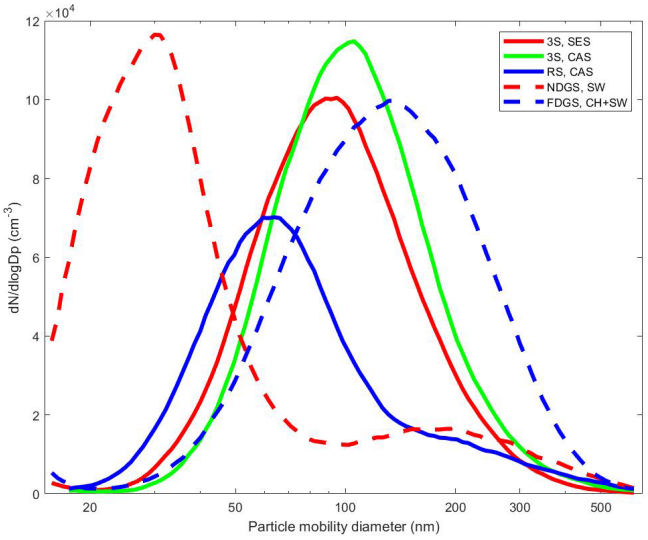

Figure 3. Examples of particle mobility size distributions from chamber experiments on different cookstoves during the time when an activated fraction of 10^{-3} was observed in the SPIN.

quasi-monodisperse size-selected soot particles. We aimed for sampling the largest possible particle mobility diameter (250–500 nm), with reasonable number concentrations (30–200 cm^{-3}) resulting in minor contributions of multiply charged particles for any given experiment (see Table 2). The presented size distributions represent the situation when an activated fraction of 10^{-3} was observed in the SPIN in each shown cookstove and fuel combination. Particles larger than 250 nm accounted for up to 15 % of the total number concentration in all chamber experiments involving the SPIN, which indicates that large soot particles were present in all studied cases.

The IN efficiencies of the emissions are presented in the following paragraphs. All experiment results are presented when a 10^{-3} activated fraction was observed during the first ascending T ramp, after the particle storage period in the chamber has been close to 1 h. The bias regarding the activated fraction due to restrictions in real-life CFDC instruments is discussed separately in Sect. 3.4 along with reproducibility of the observations.

Starting from the simplest cookstove concept, the 3S produced 10^{-3} ice activation between −37.8 and −38.6 °C (see Table 3). Although these values are close to the observed homogeneous freezing temperature, comparison to a similar experiment on diluted AS droplets reveals that ice onset due to homogeneous freezing occurs at −38.9 °C with this operation of the SPIN. The observed homogeneous freezing with 10^{-3} ice activation at an average lamina temperature of −38.9 °C may occur at a slightly lower temperature than expected from previous results reported in the literature. It is not clear at which temperature homogeneous freezing in SPIN can be expected based alone on theoretical considerations. This is due to the sample aerosol being exposed to a span in temperature and RH and uncertainties related to droplet sizes and residence times above the evaporation section as discussed by Ignatius et al. (2016). We ascribe this relatively lower and reproducible homogeneous freezing temperature for the current version of SPIN to highly improved temperature control relative to earlier versions of SPIN (Ignatius et al., 2016). Potential biases and errors are discussed in more detail later.

Figure 4 shows the results on two fuels, CAS and SES, combusted with the 3S, and three different sample sizes. The errors related to the average lamina temperature are presented above as the maximum span from the ideal lamina temperature, based on the uppermost 13 pairs of thermocouples on the warm and cold plates, respectively (Garimella et al., 2016). The statistical uncertainty of the activated fraction (vertical error bars) was found to be more prominent with low α values close to 10^{-4}; in general, this uncertainty was on the order of 10 %–20 % when the activated fraction was above 10^{-3}, which agrees with values reported by Garimella et al. (2017). The uncertainty analyses confirm that there is a significant difference in 10^{-3} onset temperatures between the 3S experiments and the homogeneous freezing experiment. Good experiment reproducibility (see Table 3) that will be discussed in Sect. 3.4 indicates very good agreement between repeated ramps and thus strengthens the validity of these observations. Size dependency that could be distinguished from the instrument uncertainty between 250, 300 and 500 nm particles was not observed, which may be due to differences in physico-chemical properties between the individual experiments.

The RS emissions were slightly more active INPs than the ones from the 3S; the 10^{-3} activated fraction was achieved between −37.9 and −38.1 °C, which is 0.8–1.0 °C higher than observed homogeneous freezing in the AS experiment, as can be seen from Table 3. Indications of size dependency were also not observed in these experiments. The results from regular gasifier stove experiments are presented in Fig. 5, and conditions for ice onset were reached at −37.8 °C on the FDGS with CH + SW pellets and at −38.1 °C on the NDGS with SW pellets during standard operation conditions. Once again, a clear size dependency was not observed; the 260 nm particles from the experiment on the FDGS appear to be slightly more IN active than 400 nm particles from the NDGS. When compared to standard tests on the 3S and the RS, these observations consistently show that the soot particles emitted from burning the various fuels can act as heterogeneous INPs at temperatures only slightly higher than those needed for homogeneous freezing of solution droplets.

The results from the five special experiments with modified combustion conditions are presented in Fig. 6. Two of the samples induced heterogeneous ice nucleation at temperatures about 4 °C (blocked secondary air supply) and 6 °C (elevated pot height) higher than observed for homogeneous freezing and an ice-active fraction of 10^{-3}, respec-

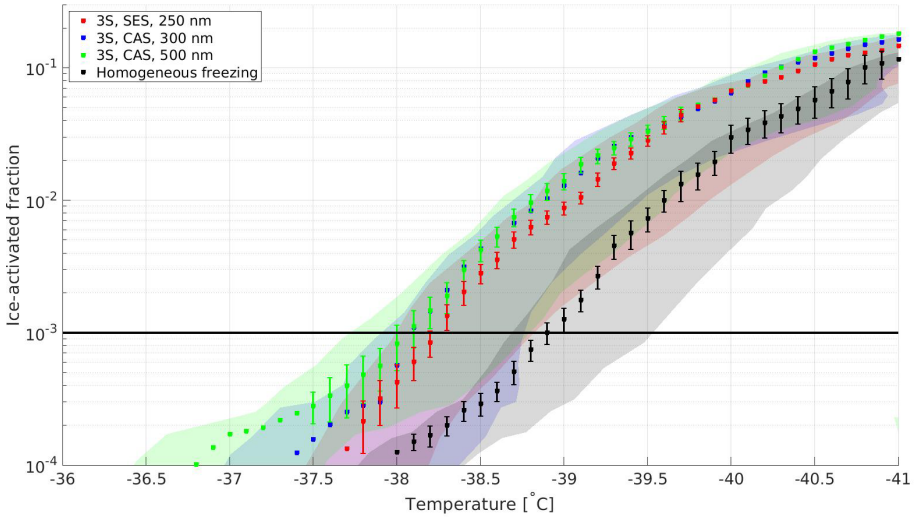

Figure 4. Ice-activation spectra of emissions from the three-stone fire at $RH_w = 115\,\%$ chamber experiments. Each shaded area represents the T span across the lamina (maximum uncertainty) during each observation. The error bars present combined relative standard deviations in particle detection by the CPC and OPC of the SPIN. The solid black line presents the 10^{-3} activation threshold. The ice-activation spectrum for homogeneous freezing is included for comparison.

Table 3. Ice onset (10^{-3} activation) temperatures when ascending temperature ramps were repeated during each chamber experiment, calculated from background-corrected signal. The last entry shows results from repeated ramps in the homogeneous freezing test. The uncertainties are equal to ± 1 standard deviation in the lamina temperature at the moment of detection. The pot height experiments represent modified combustion conditions when the cooking pot was intentionally placed above the designated height of the respective cookstove. Acronyms ND and FD refer to natural draft and forced draft, respectively.

Cookstove	Fuel	Sample size (nm)	Ice onset T (°C), ramp no. 1	Ice onset T (°C), ramp no. 2	Ice onset T (°C), ramp no. 3
Three-stone fire	SES	250	-38.3 ± 0.2	-38.2 ± 0.2	-38.2 ± 0.4
Three-stone fire	CAS	300	-38.3 ± 0.5	-38.2 ± 0.3	-38.6 ± 0.4
Three-stone fire	CAS	500	-37.8 ± 0.3	-38.0 ± 0.2	-38.1 ± 0.3
Rocket stove	CAS	250	-38.2 ± 0.3	-38.1 ± 0.3	–
Rocket stove	CAS	350	-37.8 ± 0.3	-38.1 ± 0.3	–
Rocket stove	CAS	450	-37.9 ± 0.4	-37.9 ± 0.3	–
ND gasifier	SW	400	-38.2 ± 0.3	-38.2 ± 0.3	–
FD gasifier	CH + SW	260	-37.8 ± 0.3	-38.1 ± 0.3	–
Modified FD gasifier	SW	450	-34.7 ± 0.3	-35.1 ± 0.4	-35.1 ± 0.4
Modified FD gasifier	SW	500	-38.1 ± 0.3	–	–
FD gasifier, pot height no. 1	SW	400	-33.4 ± 0.3	-33.9 ± 0.3	-34.0 ± 0.3
FD gasifier, pot height no. 2	SW	400	-38.9 ± 0.4	-38.9 ± 0.4	–
FD gasifier, pot height no. 3	SW	500	-39.3 ± 0.4	–	–
–	AS	350	-38.9 ± 0.3	-39.1 ± 0.3	-38.9 ± 0.3

tively. These experiments were repeated, and the ice activity was comparable to homogeneous freezing for other intendedly identical experiments. This indicates that very minor changes in combustion conditions significantly influence the ice-nucleating ability of freshly produced soot particles.

3.3 Properties of the emission particles

Figure 7 presents six different physico-chemical particle properties for the aerosol samples included in Fig. 6. The CCN activity was presented as the apparent κ (κ_a) and the effective density (ρ_{eff}) that were inferred for particles with a mobility diameter of 350 nm, and the results are presented in the two upper panels of Fig. 7. The κ_a values are very low for all the samples with only minor variations, and the ρ_{eff} values are also low for all the samples with minor variations. These values of ρ_{eff} (0.2–0.3) are typical for fractal-like rBC-dominated agglomerates from several different sources (Rissler et al., 2013). We observed a tendency towards de-

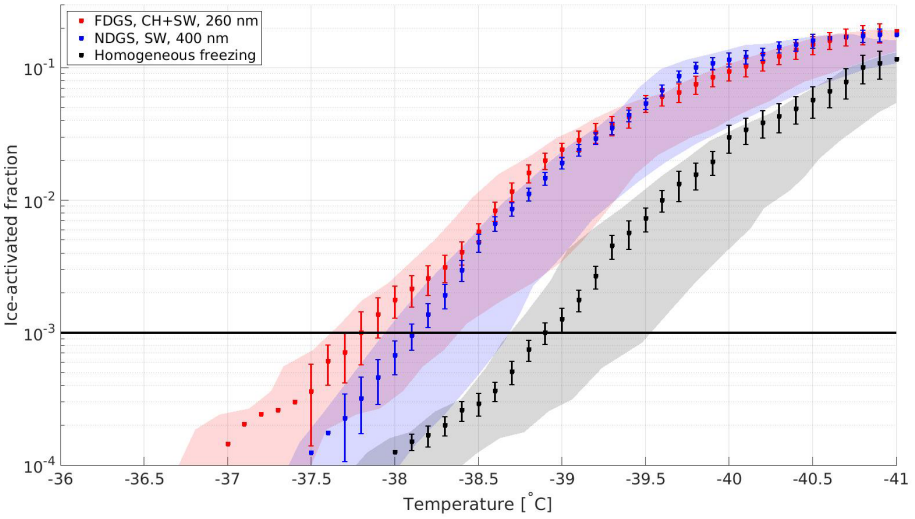

Figure 5. Ice-activation spectra of emissions from gasifier stoves at $RH_w = 115\,\%$ at regular operation conditions. Each shaded area of respective color represents the T span across the lamina (maximum uncertainty) during each observation. The error bars present combined relative standard deviations in particle detection by the CPC and OPC of the SPIN. The solid black line presents the 10^{-3} activation threshold. The ice-activation spectrum for homogeneous freezing is included for comparison.

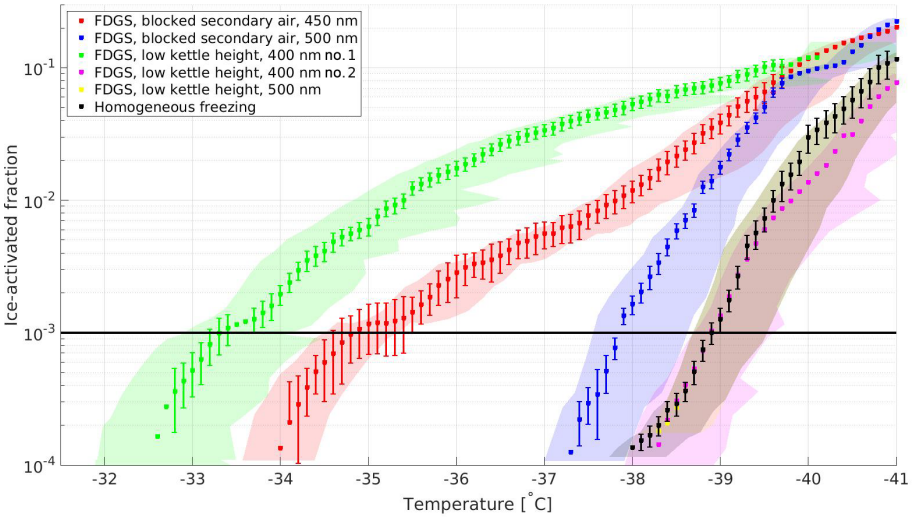

Figure 6. Ice-activation spectra of emissions from combustion of SW pellets in forced-draft gasifier stove, with modified combustion conditions at $RH_w = 115\,\%$. Each shaded area of respective color represents the T span across the lamina (maximum uncertainty) during each observation. The error bars present combined relative standard deviations in particle detection by the CPC and OPC of the SPIN. The solid black line presents the 10^{-3} activation threshold. The ice-activation spectrum for homogeneous freezing is included for comparison.

creasing κ_a and ρ_{eff} with an increasing mobility diameter in the soot mode throughout the campaign, so the presented values can be considered upper estimates of what may be relevant for the larger quasi-monodisperse soot particles studied with SPIN. The differences in κ_a and ρ_{eff} reported for a mobility size of 350 nm are expected to be representative for relative differences for the entire soot mode, which is supported by strong correlations between these properties inferred for 200 and 350 nm soot particles and further supported by the power law models for ρ_{eff} with respect to soot particles as presented by Rissler et al. (2013). Information about optical properties (AAE in the wavelength interval 370 to 950 nm), relative abundance of refractory oxygen species ($C_3O_2^+/C_3^+$), the ratio of organic aerosol mass (OA) (in the m/z range of 13–330 Th) to rBC mass and indirect information about the nanostructure (C_{mid}/C_{all}) of the polydisperse aerosol is presented in the lower panels in Fig. 7, with the three latter properties being inferred from the SP-AMS data.

It is noteworthy that both cases with blocked secondary air supply (sample sizes in 450 and 500 nm) showed ele-

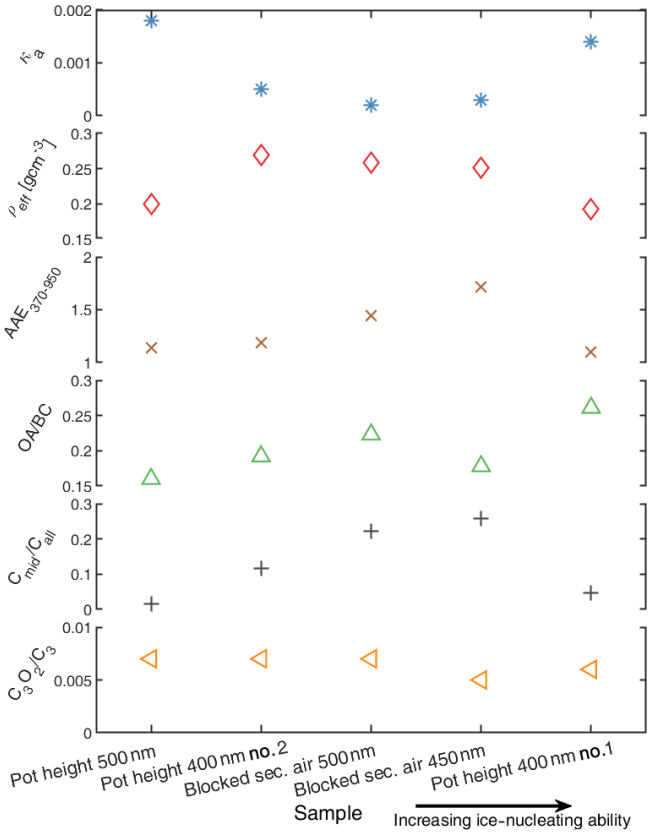

Figure 7. Physico-chemical properties of soot particles in special experiments where the combustion conditions of SW in the FDGS were modified. The five aerosol samples presented have been re-ordered in a way that the samples with higher ice-nucleating ability are located further to the right. The properties from the top to the bottom represent the CCN activity (κ_a), the effective density (ρ_{eff}), absorption Ångström exponent in the wavelength interval 370 to 950 nm ($AAE_{370-950}$), the ratio of organic aerosol mass to refractive BC mass (OA / BC), indirect qualitative information about the nanostructure (C_{mid}/C_{all}) and the relative abundance of refractory oxygen species ($C_3O_2^+/C_3^+$). The two uppermost panels are for quasi-monodisperse soot particles with a mobility diameter of 350 nm, while the other properties are inferred for polydisperse aerosol.

vated absorption in the UV region (elevated AAE) despite the low OA-to-BC ratios. These two cases were also associated with an increased fraction of carbon fragments in the mid-carbon range C_6^+ to C_{29}^+ in the refractory carbon mass spectrum detected upon laser vaporization with the SP-AMS. Malmborg et al. (2019) and Török et al. (2018) linked increased UV absorption to the occurrence of large carbon fragments in the SP-AMS mass spectrum, decreased fringe length detected by high-resolution transmission electron microscopy (HR-TEM) and refractory (partly pyrolyzing) organic carbon in thermal-optical analysis for emissions from the Mini-CAST flame soot generator. These findings suggest that such relationships are also present for refractory carbon-dominated particles from cookstoves. Particularly, the two experiments with blocked secondary air inlet in the FDGS facilitated emissions of refractory carbon species with elevated UV absorption. The ratio of $C_3O_2^+/C_3^+$ showed only small variations between experiments (0.0059–0.0069), suggesting that the occurrence of refractory oxygen species (for example surface oxides) did not vary much between experiments.

Our detailed aerosol characterization presented in Fig. 7 indicates that we did produce particles with slightly different properties for intendedly identical experiments, as also was indicated by the observed difference in the ice-nucleating ability. The low hygroscopicity, the low effective density and the optical properties indicate that the studied soot particles were not covered or coated by significant amounts of soluble material despite the presence of some organic compounds. It is noteworthy that the two more ice-active soot samples (450 nm on blocked secondary air supply and the first repetition of the pot height experiment with 400 nm) are significantly different with regards to several properties. The only minor visible trend with ice activity is a slightly lower ratio of refractory oxygen species ($C_3O_2^+/C_3^+$) for the two more ice-active soot samples relative to the less ice-active samples. However, that trend is not significant in a direct comparison to the freezing temperatures, and the differences in refractory oxygen species between the samples are not significant considering the errors. In general, these supportive data indicate that either (i) the inferred properties do not determine the ice-nucleating ability or (ii) there is a potential for complex combinations of different soot particle properties being of relevance for the ice-nucleating ability. Additional studies are needed to address these questions in more detail.

3.4 Experiment reproducibility and bias in ice crystal detection

In this section, we discuss the reproducibility of the observations to validate the results and to evaluate the measurement precision of the SPIN. The results from repeated ramps are summarized in Table 3, where we present the ice onset temperatures and their uncertainties at the lamina T. Unlike in Figs. 4–6, we present the uncertainty as 1 standard deviation from the average lamina T in this context to show the overall precision of the temperature control. Observation no. 1, no. 2 and no. 3 represent the IN onset after chamber residence times of approximately 20, 40 and 60 min, respectively, after filling the chamber was completed. These comparisons show that the results from repeated ramps are generally in good agreement with each other, and the differences in onset temperature remain within the typical deviation of the SPIN (see Sect. 2.3). It can be expected that the most prominent chamber effect has been coagulation of the ultrafine particles to large soot particles, but this has not affected the ice-nucleating ability.

It should also be mentioned that across the width of the lamina, there is an additional span in temperature typically on the order of ±0.4 °C, so a fraction of the aerosol will be exposed to further lower or higher temperatures compared to just the variability in average lamina temperature as presented in Fig. 2. However, we find that the variability in average lamina temperature is a reasonable estimate of the error in sample temperature for the experiments presented in Figs. 4–6, considering the high reproducibility of the results presented in Table 3.

Furthermore, the ice-active fraction is in the current study biased low for two reasons: (i) only a fraction of the sample aerosol is focused in the lamina (Garimella et al., 2017), and (ii) only the larger-size fraction of the ice crystals (optical diameter > 6 µm) is included in the ice-active fraction (Fig. 2). Garimella et al. (2017) reported the fraction of sample particles being focused in the lamina for comparable operation conditions of SPIN to be from 10 % to 30 % in most cases. In our homogeneous freezing experiment, the "raw" ice-activated fraction as presented in Fig. 4, for example, is about 0.12 for an average lamina temperature of −41 °C. At that temperature, we would ideally expect an ice-activated fraction close to 1, which would be reached applying a correction factor of 8 in that case. For slightly higher lamina temperatures, the correction factor could potentially be lower, so we consider a correction factor in the range from 3 to 8 to be possible for this experiment for the lamina temperature in the range from −41 to −38.0 °C. Application of such correction factors for the homogeneous freezing experiment will result in 10^{-3} ice activation between −38.5 and −38.0 °C in average lamina temperature.

The presented ice-active fractions are biased low for two main reasons, as mentioned above. As can be seen from Figs. 4–6, the ice-active fractions for a temperature of −41 °C are typically on the order of 0.1 to 0.2, while we would expect an ice-active fraction close to 1 for homogeneous freezing at that temperature below −40 °C. These observations confirm that the presented ice-active fractions are biased low. Previous studies show that only a fraction of the sample aerosol is focused in the lamina. DeMott et al. (2015) found that the ice-active fraction for mineral dust particles should be upscaled on average by a correction factor of about 3 for a CFDC over a range of operation conditions including approximately similar operation conditions (e.g., $T \approx -35$ °C and RH_w of about 106 %–108 % at the lamina) to what we apply in our study. However, for those specific operation conditions (lamina $T = -35$ °C and just before droplet break through with an expected RH_w of about 106 %–108 %) there is quite some scatter in the appropriate correction factor, and a larger correction factor is often observed (DeMott et al., 2015). The offset can be ascribed to only a fraction of the sample particles being focused on the lamina. Garimella et al. (2017) reported upscaling factors for SPIN in the range from 1.5 to 10 depending on the operation conditions due to only a fraction of the sample aerosol being focused in the lamina. This is also evident in this study at laminar temperatures below −40 °C, when all droplets are expected to freeze homogeneously: the maxima of the inferred activated fractions (see Figs. 4–6) are between approximately 0.07 and 0.2, which indicates that correction factors in the range from 5 to 13 may be of relevance for our approach and these specific conditions at low temperatures.

In the current study, we observed droplets and ice crystals coexisting after the evaporation section for a significant range of conditions, and with our established ice crystal threshold (optical diameter > 6 µm), only a (varying) fraction of the ice crystals were included in our reported ice-active fractions. The ice crystal size modes had maxima close to an optical diameter of 8 µm in the T-scan experiments, and a fraction of the ice crystal size mode would be present below 6 µm, potentially overlapping with the droplet mode. Lognormal distributions were fitted to the ice crystal size mode for different lamina temperatures higher than −36 °C for the most ice-active sample studied in order to estimate the fraction of ice crystals with optical sizes below 6 µm. We find that the ice-active fraction defined from the 6 µm threshold would have to be multiplied by a factor of $1.4 + 0.2$ in order to obtain a reasonable estimate of the ice-activated fraction considering the entire ice crystal size mode – when the ice crystal mode was observed to be well-defined and ascribed to heterogeneous immersion freezing. The uncertainty range is inferred from a sensitivity study including a range of reasonable fits, and it is due to noise in the data. It is not clear to which extent this correction factor is independent from the correction factor related to the sample aerosol not being entirely focused in the lamina. In any case, the bias associated with a relatively high ice size threshold is likely to be significantly lower than the expected bias due to only a fraction of the sample being focused in the lamina.

The underestimation based on the size threshold of 6 µm turned more significant when the sample temperature was low enough to induce freezing of droplets smaller than 3–4 µm and/or possibly hydrated particles appearing at sizes well below the ice crystal threshold. Investigation of the depolarization ratio of particles with an optical diameter in the sub-micrometer range with the SPIN OPC confirms that ice dominates in this size range at the lowest temperatures < -40 °C. Hence, the ice-active fraction inferred from our procedure is underestimated, which is likely to be significantly more pronounced in the lowest temperature, as can be seen from Fig. 2. Furthermore, the ice-active fraction may also be underestimated due to (i) losses of ice crystals immediately above the OPC, which to our knowledge have not been studied in detail so far for SPIN, and (ii) a relatively small fraction of particles activating into droplets inside SPIN – leading to a reduced fraction for detection in the immersion mode. The potential losses have to our knowledge not yet been characterized in detail – while the ice-active fractions observed for homogeneous freezing of dilute ammonium sulfate droplets and droplets formed on hydrophobic

particles typically resulted in very similar ice-active fractions (e.g., Fig. 6).

The considerations discussed above lead us to estimate a likely upscaling factor on the order of $\sim$ 3–5 of the ice-active fraction for lamina temperatures around $-33\,^{\circ}$C, while the upscaling factor is likely to approach 5–10 for temperatures significantly below homogenous freezing, around $-40\,^{\circ}$C. Further studies are needed to assess these biases in more detail – and their relative importance for different operation conditions of the CFDC instrument.

4 Summary and conclusions

The SUSTAINE experiment campaign provided an excellent opportunity to study the IN efficiencies of emissions from different biomass-fired cookstove designs under well-controlled laboratory conditions, which enabled comparability between individual experiments. Two cookstoves, the 3S and RS, represented designs that are commonly used in daily household cooking in sub-Saharan Africa. The two more sophisticated designs, the NDGS and the FDGS, are currently under research for sustainable development, and their popularity can be expected to increase along with economic development in this region and similar regions. Based on observations from five special experiments on FDGS, this study shows that even small changes in combustion conditions can significantly affect the IN abilities of emission particles. Extensive regional usage of cookstoves suggests that the solid-biomass-burning emissions from cookstoves are a significant source of atmospheric particulate matter in sub-Saharan Africa. The CFDC instrument in this study, the SPIN, showed relatively good performance in temperature control, which enabled high reproducibility of experiments.

We conclude that the studied polydisperse aerosol emissions from transient experiments with different cookstoves showed no indication of heterogeneous freezing above the detection limit (ice-activated fraction of about 10^{-5}) for the investigated conditions ($T = -28$ and $-32\,^{\circ}$C and $\sim 75\,\%$–$105\,\%$ RH_w). However, it should be kept in mind that those aerosol emissions typically were heavily dominated by ultrafine particles by number. Hence, the measurement sensitivity with respect to the accumulation mode particles alone was relatively low in those experiments. Therefore, we also carried out a number of immersion freezing experiments focused on size-selected accumulation mode soot particles sampled from an aerosol-storage chamber. The results from chamber experiments on accumulation mode soot particles show that they can induce heterogeneous ice nucleation in higher temperatures than what is required for homogeneous freezing, as happened in most of the experiments. Therefore, we conclude that usage of the cookstoves can emit potential INPs in the atmosphere and thus affect cloud properties such as the frozen fraction in low-temperature MPCs. The chamber experiments also support the outcome of transient experiments that included the same cookstove–fuel combinations because the experimental procedures included sampling at corresponding RH_w of 115 % but in lower temperatures. With these observations combined, we conclude that the fresh cookstove emissions that were tested both transiently and from the chamber do not contain components that are active INPs above a temperature of $-32\,^{\circ}$C. All but two chamber experiments show an obvious difference to homogeneous freezing experiment, and therefore these emissions may well be of relevance for INP number concentrations in regions where other sources of ambient INPs are absent. Despite the chamber experiments consistently showing IN activity above the homogeneous freezing temperature, it still needs to be noted that the studied emissions were relatively fresh: atmospheric aging processes can affect the IN properties (Brooks, et al., 2014) before the emissions reach the upper atmosphere, as is supported by Häusler at al. (2018). The effect of atmospheric aging can be studied via using, for example, oxidation reactors in future studies.

Deterioration of combustion efficiency was observed to increase the INP potential of the emission particles, which is likely due to elevated large soot particle production in incomplete combustion of the tested biomass fuels. This, when combined with results from transient experiments and ones with standard combustion conditions, indicates that even modest changes in combustion efficiency can drastically alter the ice-nucleating capabilities of the emissions. Our analysis on physico-chemical properties of the emissions revealed that the soot particle non-refractory organic coating, carbon nanostructure and light absorption characteristics were different between the least and the most ice-active results, yet none of these properties could define the IN efficiency alone. We recommend further studies that aim to investigate the relationships between the soot potential as INPs and soot nanostructure, refractory surface-bound oxygen, and non-refractory organic composition and coating thickness. It is clearly a possibility that the IN efficiency of soot is determined by a complex combination of multiple particle properties. It is therefore possible that co-correlated microphysical changes in the soot structure (on the order of 10–1000 nm) blurred the effects from changes in the non-refractory organic composition, nanostructure or oxygen bound to the soot surfaces.

It is worth emphasizing that all experiments of this study were carried out in well-controlled laboratory conditions and using standardized test procedures. Contrary to that, real-life use can differ significantly from these experiments in many factors, such as in fuel pre-processing, fuel properties, technical stove conditions and practical cooking procedures. These all affect the combustion and emission performance that can have a prominent effect on ice-nucleating abilities of emitted aerosol particles, which this study shows. Therefore, the difference between these observations and real-life use should be explored before the contribution of biomass-

burning emissions can be further evaluated in global perspective.

Data availability. The data set is available upon request from Kimmo Korhonen (kimmo.korhonen@uef.fi).

Author contributions. TBK planned the ice-nucleation experiments on the SPIN instrument that was operated by KK during the campaign. AV, JF, KK, MK and TBK participated in data analysis of ice-nucleation experiments and/or interpretation of results. RL and RLC prepared the experimental setup for water boiling tests and operated the combustion facility during the campaign. AE, CA, JF, JP, TBK and VM participated in collection of supportive data and/or interpretation of results. BS, CB and JP participated as the organizers and supervisors of the SUSTAINE experiment campaign. AV and KEJL achieved funding for the SPIN instrument. All authors participated in scientific discussions on this study and reviewed and edited the paper during its preparation process. KK prepared the paper, with contributions from all co-authors.

Competing interests. The authors declare that they have no conflict of interest.

Acknowledgements. This work was financially supported by the Swedish Research Council FORMAS through the project Sustainable Biomass Utilization in sub-Saharan Africa for an Improved Environment and Health (grant no. 942-2015-1385) and Atmospheric cloud droplet formation and ice formation of wood combustion aerosols (grant no. 2015-992). Thomas Bjerring Kristensen gratefully acknowledges funding from the Swedish Research Council (VR) grant no. 2017-05016. LU-EAT researchers acknowledge financial support from the Swedish Research Councils VR (grant nos. 2018-04200 and 2013-05021) and FORMAS (grant no. 2013-01023). The University of Eastern Finland and Finnish Meteorological Institute acknowledge the Academy of Finland, Centre of Excellence (grant no. 272041), and North-Savo Council of the European Regional Development Fund (grant no. A32350).

Financial support. This research has been supported by the Svenska Forskningsrådet Formas (grant nos. 942-2015-1385, 2015-992 and 2013-01023), the Vetenskapsrådet (grant nos. 2017-05016, 2018-04200 and 2013-05021), the Academy of Finland, Luonnontieteiden ja Tekniikan Tutkimuksen Toimikunta (grant no. 272041), and the Kempestiftelserna (grant no. JCK-1516).

Review statement. This paper was edited by Allan Bertram and reviewed by two anonymous referees.

References

Bhandari, J., China, S., Chandrakar, K. K., Kinney, K., Cantrell, W., Shaw, R. A., Mazzoleni, L. R., Girotto, G., Sharma, N., Gorkowski, K., Gilardoni, S., Decesari, S., Facchini, M. C., Zanca, N., Pavese, G., Esposito, F., Dubey, M. K., Aiken, A. C., Chakrabarty, R. K., Moosmüller, H., Onasch, T. B., Zaveri, R. A., Scarnato, B. V., Fialho, P., and Mazzoleni, C.: Extensive Soot Compaction by Cloud Processing from Laboratory and Field Observations, Sci. Rep., 9, 11824, https://doi.org/10.1038/s41598-019-48143-y, 2019.

Bond, T. C., Doherty, S. J., Fahey, D. W., Forster, P. M., Berntsen, T., DeAngelo, B. J., Flanner, M. G., Ghan, S., Kärcher, B., Koch, D., Kinne, S., Kondo, Y., Quinn, P. K., Sarofirm, M. C., Schultz, M. G., Schulz, M., Venkataraman, C., Zhang, H., Zhang, S., Bellouin, N., Guttikunda, S. K., Hopke, P. K., Jacobson, M. Z., Kaiser, J. W., Klimont, Z., Lohmann, U., Schwarz, J. P., Shindell, D., Storelvmo, T., Warren, S. G., and Zender, C. S.: Bounding the role of black carbon in the climate system: A scientific assessment, J. Geophys. Res.-Atmos., 118, 5380–5552, https://doi.org/10.1002/jgrd.50171, 2013.

Bonjour, S., Adair-Rohani, H., Wolf, J., Bruce, N. G., Mehta, S., Prüss-Ustün, A., Lahiff, M., Rehfuess, E. A., Mishra, V., and Smith, K. R.: Solid fuel use for household cooking: Country and regional estimates for 1980–2010, Environ. Health Perspect., 121, 784–790, https://doi.org/10.1289/ehp.1205987, 2013.

Boucher, O., Randall, D., Artaxo, P., Bretherton, C., Feingold, G., Forster, P., Kerminen, V.-M., Kondo, Y., Liao, H., Lohmann, U., Rasch, P., Satheesh, S. K., Sherwood, S., Stevens, B., and Zhang, X. Y.: Clouds and Aerosols, in: Climate Change 2013: The Physical Science Basis, Contribution of Working Group I to the Fifth Assessment Report of the Intergovernmental Panel on Climate Change, edited by: Stocker, T. F., Qin, D., Plattner, G.-K., Tignor, M., Allen, S. K., Boschung, J., Nauels, A., Xia, Y., Bex, V., and Midgley, P. M., Cambridge University Press, Cambridge, United Kingdom and New York, NY, USA, 2013.

Brooks, S. D., Suter, K., and Olivarez, L.: Effects of Chemical Aging on the Ice Nucleation Activity of Soot and Polycyclic Aromatic Hydrocarbon Aerosols, J. Phys. Chem. A, 118, 10036–10047, https://doi.org/10.1021/jp508809y, 2014.

Carvalho, R. L., Jensen, O. M., and Tarelho, L. A. C.: Mapping the performance of wood-burning stoves by installations worldwide, Energ. Building., 127, 658–679, https://doi.org/10.1016/j.enbuild.2016.06.010, 2016.

Carvalho, R. L., Lindgren, R., García-Lópeza, N., Nyambane, A., Nyberg, G., Diaz-Chavez, R., and Boman, C.: Household air pollution mitigation with integrated biomass/cookstove strategies in Western Kenya, Energ. Pol., 131, 168–186, https://doi.org/10.1016/j.enpol.2019.04.026, 2019.

Champion, W. M. and Grieshop, A. P.: Pellet-Fed Gasifier Stoves Approach Gas-Stove Like Performance during in-Home Use in Rwanda, Environ. Sci. Tech., 53, 6570–6579, https://doi.org/10.1021/acs.est.9b00009, 2019.

Chou, C., Stetzer, O., Weingartner, E., Jurányi, Z., Kanji, Z. A., and Lohmann, U.: Ice nuclei properties within a Saharan dust event at the Jungfraujoch in the Swiss Alps, Atmos. Chem. Phys., 11, 4725–4738, https://doi.org/10.5194/acp-11-4725-2011, 2011.

Corbin, J. C., Lohmann, U., Sierau, B., Keller, A., Burtscher, H., and Mensah, A. A.: Black carbon surface oxidation and organic composition of beech-wood soot aerosols, Atmos. Chem.

Phys., 15, 11885–11907, https://doi.org/10.5194/acp-15-11885-2015, 2015.

DeMott, P.: An exploratory study of ice nucleation by soot aerosols, J. Appl. Meteorol., 29, 1072–1079, 1990.

DeMott, P. J., Prenni, A. J., Liu, X., Kreidenweis, S. M., Petters M. D., Twohy, C. H., Richardson, M. S., Eidhammer, T., and Rogers, D. C.: Predicting global atmospheric ice nuclei distributions and their impacts on climate, P. Natl. Acad. Sci. USA, 107, 11217–11222, https://doi.org/10.1073/pnas.0910818107, 2010.

DeMott, P. J., Prenni, A. J., McMeeking, G. R., Sullivan, R. C., Petters, M. D., Tobo, Y., Niemand, M., Möhler, O., Snider, J. R., Wang, Z., and Kreidenweis, S. M.: Integrating laboratory and field data to quantify the immersion freezing ice nucleation activity of mineral dust particles, Atmos. Chem. Phys., 15, 393–409, doi:10.5194/acp-15-393-2015, 2015.

DeMott, P. J., Hill, T. C. J., Petters, M. D., Bertram, A. K., Tobo, Y., Mason, R. H.,Suski, K. J., McCluskey, C. S., Levin, E. J. T., Schill, G. P., Boose, Y., Rauker, A. M., Miller, A. J., Zaragoza, J., Rocci, K., Rothfuss, N.E., Taylor, H. P., Hader, J. D., Chou, C., Huffman, J. A., Pöschl, U., Prenni, A. J., and Kreidenweis, S. M.: Comparative measurements of ambient atmospheric concentrations of ice nucleating particles using multiple immersion freezing methods and a continuous flow diffusion chamber, Atmos. Chem. Phys., 17, 11227–11245, https://doi.org/10.5194/acp-17-11227-2017, 2017.

Diehl, K. and Mitra, S. K.: A laboratory study of the effects of a kerosene-burner exhaust on ice nucleation and the evaporation rate of ice crystals, Atmos. Environ., 32, 3145–3151, 1998.

Ferry, D., Suzanne, J., Nitsche, S., Popovicheva, O. B., and Shonija, N. K.: Water adsorption and dynamics on kerosene soot under atmospheric conditions, J. Geophys. Res., 107, D234734, https://doi.org/10.1029/2002JD002459, 2002.

Food and Agriculture Organization of the United Nations: Agroforestry for landscape restoration, Rome, 5–10, 2017.

Garimella, S., Kristensen, T. B., Ignatius, K., Welti, A., Voigtländer, J., Kulkarni, G. R., Sagan, F., Kok, G. L., Dorsey, J., Nichman, L., Rothenberg, D., Rösch, M., Kirchgäßner, A., Ladkin, R., Wex, H., Wilson, T. W., Ladino, L. A., Abbatt, J. P. D., Stetzer, O., Lohmann, U., Stratmann, F., and Cziczo, D. J.: The Spectrometer for Ice Nuclei (SPIN): An instrument to investigate ice nucleation, Atmos. Meas. Tech., 9, 2781–2795, https://doi.org/10.5194/amt-9-2781-2016, 2016.

Garimella, S., Rothenberg, D. A., Wolf, M. J., David, R. O., Kanji, Z. A., Wang, C., Rösch, M., and Cziczo, D. J.: Uncertainty in counting ice nucleating particles with continuous flow diffusion chambers, Atmos. Chem. Phys., 17, 10855–10864, https://doi.org/10.5194/acp-17-10855-2017, 2017.

Gorbunov, B., Baklanov, A., Kakutkina, N., Windsor, H. L., and Toumi, R.: Ice nucleation on soot particles, Aerosol. Sci., 32, 199–215, https://doi.org/10.1016/S0021-8502(00)00077-X, 2001.

Häusler, T., Gebhardt, P., Iglesias, D., Rameshan, C., Marchesan, S., Eder, D., and Grothe, H.: Ice Nucleation Activity of Graphene and Graphene Oxides, J. Phys. Chem., 122, 8182–8190, doi:10.1021/acs.jpcc.7b10675, 2018.

Hoose, C. and Möhler, O.: Heterogeneous ice nucleation on atmospheric aerosols: a review of results from laboratory experiments, Atmos. Chem. Phys., 12, 9817–9854, https://doi.org/10.5194/acp-12-9817-2012, 2012.

Huang, Y., Unger, N., Storelvmo, T., Harper, K., Zheng, Y., and Heyes, C.: Global radiative effects of solid fuel cookstove aerosol emissions, Atmos. Chem. Phys., 18, 5219–5233, https://doi.org/10.5194/acp-189-5219-2018, 2018.

Ignatius, K., Kristensen, T. B., Järvinen, E., Nichman, L., Fuchs, C.,Gordon, H., Herenz, P., Hoyle, C. R., Duplissy, J., Garimella, S.,Dias, A., Frege, C., Höppel, N., Tröstl, J., Wagner, R., Yan, C.,Amorim, A., Baltensperger, U., Curtius, J., Donahue, N. M., Gallagher, M. W., Kirkby, J., Kulmala, M., Möhler, O., Saathoff, H., Schnaiter, M., Tomé, A., Virtanen, A., Worsnop, D., and Stratmann, F.: Heterogeneous ice nucleation of viscous secondary organic aerosol produced from ozonolysis of a-pinene, Atmos. Chem. Phys., 16, 6495–6509, https://doi.org/10.5194/acp-16-6495-2016, 2016.

International Coffee Organization: Coffee Market Report, September 2019, 7, 2019.

Kanji, Z., Ladino, L.A., Wex, H., Boose, Y., Burkert-Kohn, M., Cziczo, D., and Krämer, M.: Overview of Ice Nucleating Particles, Meteorol. Monogr., 58, 1–33, https://doi.org/10.1175/AMSMONOGRAPHS-D-16-0006.1, 2017.

Koehler, K. A., DeMott, P. J., Kreidenweiss, S. M., Popovicheva, O. B., Petters, M. D., Carrico, C. M., Kireeva, E. D., Khokhlova, T. D., and Shonija, N. D.: Cloud condensation nuclei and ice nucleation activity of hydrophobic and hydrophilic soot particles, Phys. Chem. Chem. Phys., 11, 7906–7920, https://doi.org/10.1039/B905334B, 2009.

Korolev, A., Farquhar, G., Field, P. R., Franklin, C., Lawson, P., Wand, Z., Williams, E., Abel, S. J., Axisa, D., Borrmann, S., Crosier, J., Fugal, J., Krämer, M., Lohmann, U., Schlenzek, O., Schnaiter, M., and Wendisch, M.: Mixed-Phase Clouds: Progress and Challenges, Meteorol. Monogr., 58, 1–50, https://doi.org/10.1175/AMSMONOGRAPHS-D-17-0001.1, 2017.

Levin, E. J. T., McMeeking, G. R., DeMott, P. J., McCluskey, C. S., Carrico, C. M., Nakao, S., Jayrathne, T., Stone, E. A., Stockwell, C. E., Yokelson, R. J., and Kreidenweis, S. M.: Ice-nucleating particle emissions from biomass combustion and the potential importance of soot aerosol, J. Geophys. Res.-Atmos., 121, 5888–5903, https://doi.org/10.1002/2016JD024879, 2016.

Lim, S. S., Vos, T., Flaxman, A. D., Danaei, G., Shibuya, K., Adair-Rohani, H., AlMazroa, M. A., Amann, M., Anderson, H. R., Andrews, K. G., Aryee, M., Atkinson, C., Bacchus, L. J., Bahalim, A. N., Balakrishnan, K., Balmes, J., Barker-Collo, S., Baxter, A., Bell, M. L., Blore, J. D., Blyth, F., Bonner, C., Borges, G., Bourne, R., Boussinesq, M., Brauer, M., Brooks, P., Bruce, N. G., Brunekreef, B., Bryan-Hancock, C., Bucello, C., Buchbinder, R., Bull, F., Burnett, R. T., Byers, T. E., Calabria, B., Carapetis, J., Carnahan, E., Chafe, Z., Charlson, F., Chen, H., Chen, J. S., Chen, A. T.-A., Child, J. C., Cohen, A., Colson, K. E., Cowie, B. C., Darby, S., Darling, S., Davis, A., Degenhardt, L., Dentener, F., Des Jarlais, D. C., Devries, K., Dherani, M., Ding, E. L., Dorsey, E. R., Driscoll, T., Edmond, K., Ali, S. E., Engell, R. E., Erwin, P. J., Fahimi, S., Falder, G., Farzadfar, F., Ferrari, A., Finucane, M. M., Flaxman, S., Fowkes, F. G., Freedman, G., Freeman, M. K., Gakidou, E., Ghosh, S., Giovannucci, E., Gmel, G., Graham, K., Grainger, R., Grant, B., Gunnell, D., Gutierrez, H. R., Hall, W., Hoek, H. W., Hogan, A., Hosgood 3rd, H. D., Hoy, D., Hu, H., Hubbell, B. J., Hutchings, S. J., Ibeanusi, S. E.,

Jacklyn, G. L., Jasrasaria, R., Jonas, J. B., Kan, H., Kanis, J. A., Kassebaum, N., Kawakami, N., Khang, Y. H., Khatibzadeh, S., Khoo, J. P., Kok, C., Laden, F., Lalloo, R., Lan, Q., Lathlean, T., Leasher, J. L., Leigh, J., Li, Y., Lin, J. K., Lipshultz, S. E., London, S., Lozano, R., Lu, Y., Mak, J., Malekzadeh, R., Mallinger, L., Marcenes, W., March, L., Marks, R., Martin, R., McGale, P., McGrath, J., Mehta, S., Mensah, G. A., Merriman, T. R., Micha, R., Michaud, C., Mishra, V., Mohd Hanafiah K., Mokdad, A. A., Morawska, L., Mozaffarian, D., Murphy, T., Naghavi, M., Neal, B., Nelson, P. K., Nolla, J. M., Norman, R., Olives, C., Omer, S. B., Orchard, J., Osborne, R., Ostro, B., Page, A., Pandey, K. D., Parry, C. D., Passmore, E., Patra, J., Pearce, N., Pelizzari, P. M., Petzold, M., Phillips, M. R., Pope, D., Pope 3rd, C. A., Powles, J., Rao, M., Razavi, H., Rehfuess, E. A., Rehm, J. T., Ritz, B., Rivara, F. P., Roberts, T., Robinson, C., Rodriguez-Portales, J. A., Romieu, I., Room, R., Rosenfeld, L. C., Roy, A., Rushton, L., Salomon, J. A., Sampson, U., Sanchez-Riera, L., Sanman, E., Sapkota, A., Seedat, S., Shi, P., Shield, K., Shivakoti, R., Singh, G. M., Sleet, D.A., Smith, E., Smith, K. R., Stapelberg, N. J., Steenland, K., Stöckl, H., Stovner, L. J., Straif, K., Straney, L., Thurston, G. D., Tran, J. H., Van Dingenen, R., van Donkelaar, A., Veerman, J. L., Vijayakumar, L., Weintraub, R., Weissman, M. M., White, R. A., Whiteford, H., Wiersma, S. T., Wilkinson, J. D., Williams, H. C., Williams, W., Wilson, N., Woolf, A. D., Yip, P., Zielinski, J. M., Lopez, A. D., Murray, C. J., Ezzati, M., AlMazroa, M. A., and Memish, Z. A.: A comparative risk assessment of burden of disease and injury attributable to 67 risk factors and risk factor clusters in 21 regions, 1990–2010: a systematic analysis for the Global Burden of Disease Study 2010, Lancet, 380, 2224–60, https://doi.org/10.1016/S0140-6736(12)61766-8, 2012.

Mahrt, F., Marcolli, C., David, R. O., Grönquist, P., Barthazy Meier, E. J., Lohmann, U., and Kanji, Z. A.: Ice nucleation abilities of soot particles determined with the Horizontal Ice Nucleation Chamber, Atmos. Chem. Phys., 18, 13363–13392, https://doi.org/10.5194/acp-18-13363-2018, 2018.

Malmborg, V. B., Eriksson, A. C., Török, S., Zhang, Y., Kling, K., Martinsson, J., Fortner, E. C., Gren, L., Kook, S., Onasch, T. B., Bengtsson, P.-E., and Pagels, J.: Relating aerosol mass spectra to composition and nanostructure of soot particles, Carbon, 142, 535–546, https://doi.org/10.1016/j.carbon.2018.10.072, 2019.

Matus, A. V. and L'Ecuyer, T. S.: The role of cloud phase in-Earth's radiation budget, J. Geophys. Res.-Atmos., 122, 2559–25, https://doi.org/10.1002/2016JD025951, 2017.

McCluskey, C. S., DeMott, P. J., Prenni, A. J., Levin, E. J. T., McMeeking, G. R., Sullivan, A. P., Hill, T. C. J., Nakao, S., Carrico, C. M., and Kreidenweis, S. M.: Characteristics of atmospheric ice nucleating particles associated with biomass burning in the US: Prescribed burns and wildfires, J. Geophys. Res.-Atmos., 119, 10458–10470, https://doi.org/10.1002/2014JD021980, 2014.

Mülmenstädt, J., Sourdeval, O., Delanoë, J., and Quaas, J.: Frequency of occurrence of rain from liquid-, mixed-, and ice-phase clouds derived from A-Train satellite retrievals, Geophys. Res. Lett., 42, 6502–6509, https://doi.org/10.1002/2015GL064604, 2015.

Muthayya S., Sugimoto, J. D., Montgomery, S., and Maberlys, G. F.: An overview of global rice production, supply, trade, and consumption, Ann. Ny. Acad. Sci., 1324, 7–14, https://doi.org/10.1111/nyas.12540, 2014.

Nielsen, I. E., Eriksson, A. C., Lindgren, R., Martinsson, J., Nyström, R., Nordin, E. Z., Sadiktsis, I., Boman, C., Nøjgaard, J. K., and Pagels, J.: Time-resolved analysis of particle emissions from residential biomass combustion–Emissions of refractory black carbon, PAHs and organic tracers, Atmos. Environ., 165, 179–190, https://doi.org/10.1016/j.atmosenv.2017.06.033, 2017.

Oliveira, L. S. and Franca, A. S.: Coffee in Health and Disease Prevention – 1st Edn., chap. 31, An Overview of the Potential Uses for Coffee Husks, Coffee in Health and Disease Prevention, 283–291, https://doi.org/10.1016/B978-0-12-409517-5.00031-0, 2015.

Onasch, T. B., Trimborn, A., Fortner, E. C., Jayne, J. T., Kok, G. L., Williams, L. R., Davidovits, P., and Worsnop, D. R.: Soot particle aerosol mass spectrometer: development, validation, and initial application, Aerosol. Sci. Tech., 46, 804–817, 2012.

Petters, M. D. and Kreidenweis, S. M.: A single parameter representation of hygroscopic growth and cloud condensation nucleus activity, Atmos. Chem. Phys., 7, 1961–1971, https://doi.org/10.5194/acp-7-1961-2007, 2007.

Petters, M. D., Parsons, M. T., Prenni, A. J., DeMott, P. J., Kreidenweis, S. M., Carrico, C. M., Sullivan, A. P., McMeeking, G. R., Levin, E., Wold, C. E., Collett Jr., J. L., and Moosmüller, H.: Ice nuclei emissions from biomass burning, J. Geophys. Res., 114, D07209, https://doi.org/10.1029/2008JD011532, 2009.

Popovicheva, O., Kireeva, E., Persiantseva, N., Khokhlova, T., Shonija, N., Tishkova, V., and Demirdijan, B.: Effect of soot on immersion freezing of water and possible atmospheric implications, Atmos. Res., 90, 326–337, https://doi.org/10.1016/j.atmosres.2008.08.004, 2008.

Potgieter, L. J., Richardson, D. M., and Wilson, J. R. U.: Casuarina: biogeography and ecology of an important tree genus in a changing world, Biol. Invasions, 16, 609–633, https://doi.org/10.1007/s10530-013-0613-x, 2014.

Pruppacher, H. R. and Klett, J. D.: Microphysics of Clouds and Precipitation, Atmospheric and Oceanographic Sciences Library, Kluwer Academic Publishers, Dordrecht, the Netherlands, 192–215, 1997.

Rissler, J., Messing, M. E., Malik, A. I., Nilsson, P. T., Nordin, E. Z., Bohgard, M., Sanati, M., and Pagels, J.: Effective density characterization of soot agglomerates from various sources and comparison to aggregation theory, Aerosol. Sci. Tech., 47, 792–805, https://doi.org/10.1080/02786826.2013.791381, 2013.

Rogers, D. C.: Development of a continuous flow thermal gradient diffusion chamber for ice nucleation studies, Atmos. Res., 22, 149–181, 1988.

Stetzer, O., Baschek, B., Lüönd, F., and Lohmann, U.: The Zurich Ice Nucleation Chamber (ZINC) – a new instrument to investigate atmospheric ice formation, Aerosol Sci. Tech., 42, 64–72, 2008.

Török, S., Malmborg, V. B., Simonsson, J., Eriksson, A., Martinsson, J., Mannazhi, M., Pagels, J., and Bengtsson, P. E.: Investigation of the absorption Ångström exponent and its relation to physicochemical properties for mini-CAST soot, Aerosol. Sci. Tech., 52, 757–767, https://doi.org/10.1080/02786826.2018.1457767, 2018.

Twohy, C. H., DeMott, P. J., Pratt, K. A., Subramanian, R., Kok, G. L., Murphy, S. M., Lersch, T., Heymsfield, A. J., Wang, Z.,

Prather, K. A., and Seinfeld, J. H.: Relationships of Biomass-Burning Aerosols to Ice in Orographic Wave Clouds, J. Atm. Sci., 67, 2437–2450, https://doi.org/10.1175/2010JAS3310.1, 2010.

Vali, G., DeMott, P. J., Möhler, O., and Whale, T. F.: Technical Note: A proposal for ice nucleation terminology, Atmos. Chem. Phys., 15, 10263–10270, https://doi.org/10.5194/acp-15-10263-2015, 2015.

Vergara-Temprado, J., Holden, M. A., Orton, T. R., O'Sullivan, D., Umo, N. S., Browse, J., Reddington, C., Baeza-Romero, M. T., Jones, J. M., Lea-Langton, A., Williams, A., Carslaw, K. S., and Murray, B. J.: Is Black Carbon an Unimportant Ice-Nucleating Particle in Mixed-Phase Clouds?, J. Geophys. Res., 123, 4273–4283, https://doi.org/10.1002/2017JD027831, 2018.

Welti A., Lüönd, F., Stetzer, O., and Lohmann, U.: Influence of particle size on the ice nucleating ability of mineral dusts, Atmos. Chem. Phys., 9, 6705–6715, https://doi.org/10.5194/acp-9-6705-2009, 2009.

Wiedensohler, A.: An approximation of the bipolar charge distribution for particles in the submicron size range, J. Aerosol. Sci., 19, 387–389, https://doi.org/10.1016/0021-8502(88)90278-9, 1988.

Yun, Y., Penner, J. E., and Popovicheva, O.: The effects of hygroscopicity on ice nucleation of fossil fuel combustion aerosols in mixed-phase clouds, Atmos. Chem. Phys., 13, 4339–4348, https://doi.org/10.5194/acp-13-4339-2013, 2013.